Deep Resources Engineering 2 (2025) 100188

Contents lists available at ScienceDirect

Deep Resources Engineering

journal homepage: www.keaipublishing.com/en/journals/deepre/

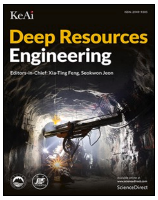

Short communication

# Analysis of physico-mechanical properties and pore structure characteristics of thermally damaged sandstone

Junqiao Yu [a], Yun Wu [a,b,*], Jiamin Wang [c,**], Lei Wang [d], Lihua Hu [b], Jian Lin [a]

[a] *Anhui Key Laboratory of Geotechnical Engineering Intelligent Construction and Disaster Prevention and Control, Hefei 230601, China*
[b] *Yunlong Lake Laboratory of Deep Underground Science and Engineering, Xuzhou 221116, China*
[c] *Academy of Deep Earth Sciences, Chinese Institute of Coal Science, Beijing 100013, China*
[d] *Institute of Geotechnical and Underground Engineering, Shandong University, Ji'nan 250061, China*

ARTICLE INFO

*Keywords:*
Underground coal gasification (UCG)
High temperature
Pore structure
Fractal dimension
Physical and mechanical properties

ABSTRACT

Under the conditions of underground coal gasification (UCG), the pore structure and mechanical properties of overlying rocks are crucial for the stability of surrounding strata. Therefore, it is of great significance to investigate the thermal damage of surrounding rocks. In this study, the variations in apparent characteristics, mass, P-wave velocity, porosity and strength of sandstone after high temperature from room temperature to 800 °C. The results indicate that the physical and mechanical properties of sandstone exhibit different degrees of variation after being subjected to high temperatures. Macropores complexity peaks at 400 °C then weakens due to crack network simplification, while mesopores regularity linearly increases with cementation loss. Porosity growth rate shows three-stage escalation through thresholds at 200 °C and 600 °C, rising from 3.81 % (25 °C) to 18.70 % (800 °C). The mechanism of sandstone damage caused by high temperatures has been explored based on microscopic thin-section analysis, and the findings of the research can offer insights for the evaluation of rock damage in underground coal gasification.

## 1. Introduction

Underground coal gasification (UCG) is a process that converts coal into combustible gases through controlled in-situ combustion, involving thermal and chemical reactions, significantly enhancing coal resource utilization [1]. As illustrated in Fig. 1, UCG generates substantial heat and combustion gases, altering the physical and mechanical properties of overlying rock strata and compromising the stability of surrounding rocks. This process may lead to ground subsidence and failure of gasifier sealing [2,3]. Consequently, understanding the effects of high temperatures on the physical and mechanical characteristics of rock masses is critical for safe and successful engineering design [4].

As temperature increases, thermal stress-induced damage to surrounding rocks intensifies [5–7]. Elevated temperatures alter the key parameters of rock mass, including mass, longitudinal wave velocity, permeability, porosity, and strength [8–12]. Under thermal stress, initial defects in rock masses-such as pores, microcracks, and fractures-evolve through the initiation, propagation, and interconnection of intergranular, transgranular, and boundary cracks, ultimately degrading rock integrity [13–17]. For instance, the physical properties of red sandstone exhibit three distinct stages of evolution with temperature: 25–300 °C, 300–800 °C, and 800–1000 °C [6]. Deng [7] observed that the uniaxial compressive strength (UCS) of sandstone initially increases and then decreases with rising temperature. These studies collectively confirm the existence of threshold temperatures beyond which rock properties deteriorate significantly.

Advancements in modern testing equipment and methodologies have enabled integrated macro-micro investigations into the thermal damage of rocks under high temperatures [18]. Current mainstream techniques include optical microscopy (OM), nuclear magnetic resonance (NMR), scanning electron microscopy (SEM), computed tomography (CT), and X-ray diffraction (XRD) [19–22]. For example, Acevedo Zamora [23] developed a novel image analysis software, "Pipeline," combined with OM, to analyze thin sections of five metamorphic rocks and standard optical microscope images, demonstrating its efficacy in mineral identification and classification. NMR is widely used to track the evolution of fine pore structures under varying environmental conditions. Zhang [18] employed NMR to study sandstone pore structure

---

* Corresponding author at: Anhui Key Laboratory of Geotechnical Engineering Intelligent Construction and Disaster Prevention and Control, Hefei 230601, China.
** Corresponding author.
*E-mail addresses:* 6780@cumt.edu.cn (Y. Wu), jasmin1029@163.com (J. Wang).

https://doi.org/10.1016/j.deepre.2025.100188
Received 14 February 2025; Received in revised form 30 April 2025; Accepted 6 May 2025

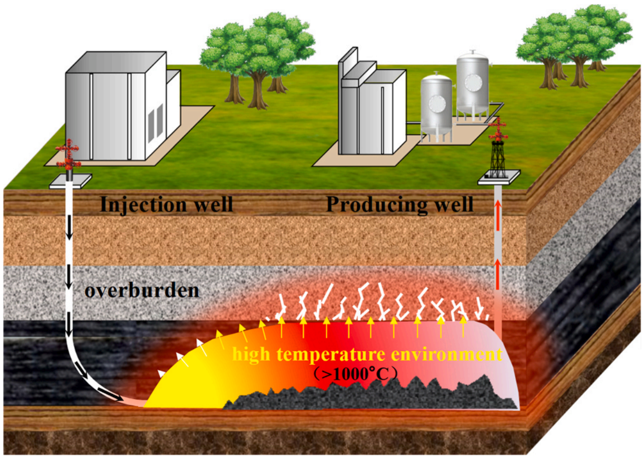

**Fig. 1.** Schematic diagram of high-temperature environment and overlying rock stability for underground coal gasification (UCG).

evolution under combined thermal and acidic conditions, revealing a gradual reduction in micropores and an increase in mesopores and macropores. Fan [24] utilized CT to analyze the microstructure, heterogeneity, and anisotropy of granite after high-temperature treatment, showing that porosity increases significantly between 400 °C and 800 °C. Yang [25] conducted in-depth CT-based studies on internal crack evolution in thermally damaged granite.

While extensive research has focused on temperature-dependent variations in rock physical and mechanical properties, existing studies predominantly emphasize macroscopic pore structure evolution and its correlation with mechanical parameters. However, the synergistic mechanisms between pore fractal characteristics and mineral composition during thermal damage remain unclear. Systematic studies integrating fractal dimension-based quantification of pore complexity, XRD mineral analysis, and thin-section microscopy are notably lacking. Therefore, a comprehensive investigation into the multi-scale coupling mechanisms governing the microstructural evolution of thermally damaged sandstone is essential to elucidate the intrinsic drivers of its physical and mechanical degradation. In the context of UCG, this study selects red sandstone as the research subject. Specimens are thermally treated at varying temperatures, and apparent characteristics, longitudinal wave velocity, and mass loss are measured. Nuclear magnetic resonance (NMR) is employed to explore pore evolution patterns under different thermal conditions, while mechanical performance is evaluated to establish theoretical and experimental foundations for assessing thermally-induced damage to surrounding rocks.

## 2. Materials and methods

### 2.1. Sample preparation

Red sandstone samples were collected from Rizhao City, Shandong Province, China (Fig. 2). The specimens exhibited a red surface with scattered white spots at room temperature. To minimize heterogeneity, all samples were extracted from a single rock block following the recommendations of the International Society for Rock Mechanics (ISRM). Standard cylindrical specimens (diameter: 50 mm; height: 100 mm or 25 mm) were prepared, totaling 20 samples. Both ends of the specimens were polished to ensure flatness with a tolerance of ± 0.2 mm. These samples were designated for Brazilian splitting tests and uniaxial compression tests. The primary mineral components of the samples are quartz (Qtz), albite (Ab), microcline (Mi), and kaolinite (Kln), with minor calcite (Cal). Specifically, $SiO_2$ content is the highest at 73.7 %, while the contents of $Na(AlSi_3O_8)$, $K(AlSi_3O_8)$, $K(Al_4Si_2O_9(OH)_3)$, and $Ca(CO_3)$ are 11.1 %, 6.9 %, 6.6 %, and 1.7 %, respectively (Fig. 3).The initial longitudinal wave velocity of the sandstone averaged 2134 m/s. Specimens were grouped and numbered based on their longitudinal wave velocity results.

**Fig. 2.** Geographic location of sandstone samples.

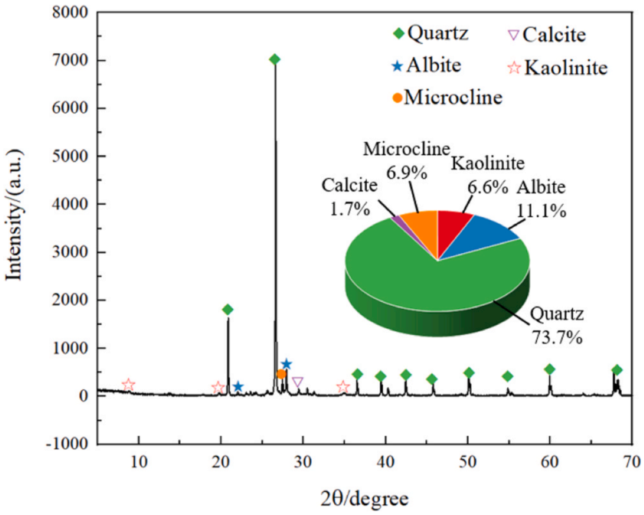

**Fig. 3.** Mineral composition analysis of sandstone at room temperature.

### 2.2. Thermal treatment

Heating rate, target temperature, cooling rate, cooling method, and medium significantly influence the physical and mechanical properties of rocks [26]. Rapid or slow heating rates affect the evolution of thermal cracks differently [27]. A TNX1400 muffle furnace (maximum temperature: 1350 °C, temperature control precision: ±1°C) was employed for heating. The furnace automatically regulated heating and cooling processes. Five temperature levels were selected: 25 °C, 200 °C, 400 °C, 600 °C, and 800 °C. Each temperature group included two parallel specimens. The heating rate was set to 5 °C/min. After reaching the target temperature, specimens were held for 4 h to ensure uniform heating. Following thermal treatment, the furnace was turned off, and specimens were naturally cooled to room temperature inside the furnace before subsequent testing.

### 2.3. Testing equipment and procedures

The testing equipment and procedures are shown in Fig. 4. After

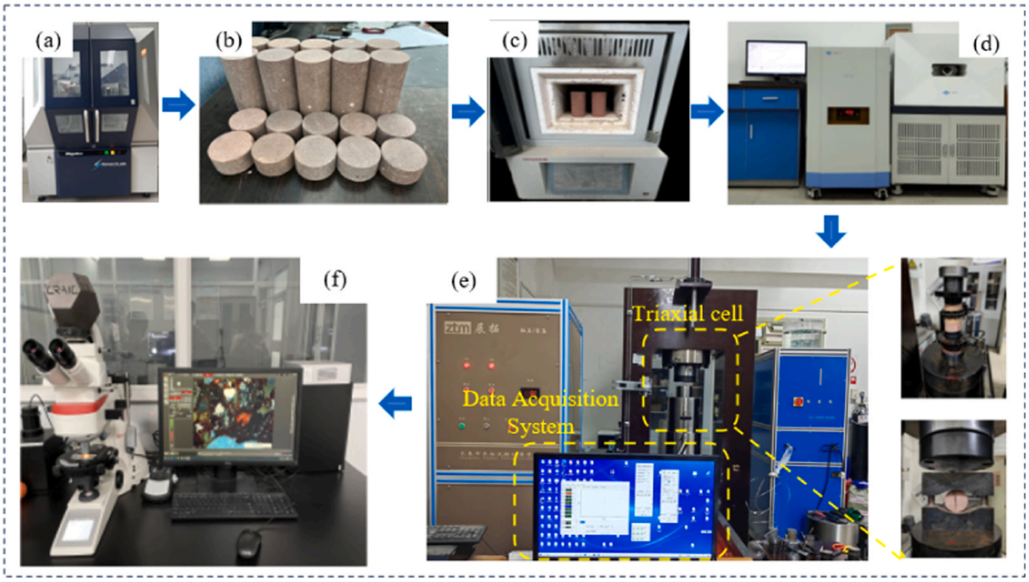

**Fig. 4.** Main experimental equipment and procedure.

thermal treatment, a D8 ADVANCE X-ray diffractometer was used for phase analysis of the original samples. The instrument has a scanning range of 0°∼140°, a goniometer precision of 0.0001°, and an accuracy $\leq 0.02°$. A high-precision analytical balance was used to measure the sample mass, with three measurements per sample. An HS-YS301T ultrasonic detector (produced by Tianhong Electronics Institute, Xiangtan) was employed to determine longitudinal wave velocity. This instrument has one transmission channel, one receiving channel, a frequency bandwidth of 10 kHz–1.5 MHz, a sampling rate of 0.05 μs, and a sampling capacity of 4k. During testing, to ensure good contact between the sample and the probe, Vaseline was evenly applied to the ultrasonic transducer, and the sample and transducer were placed together on the test bench. A MesoMR23–060V-I nuclear magnetic resonance (NMR) analyzer was used to test the porosity of the samples. First, the treated samples were placed in a water-filled container, which was then placed in a vacuum saturator for 24 h of water saturation, with dry and wet vacuum pumping each set to 4 h. After vacuum treatment, the saturated samples were removed and sealed with polytetrafluoroethylene (PTFE) film. The entire experiment adopted the Carr-Purcell-Meiboom-Gill (CPMG) sequence. The main parameters of this sequence were as follows: The magnet temperature is maintained at 32 °C with a main radiofrequency signal frequency of 21 MHz. The acquisition parameters

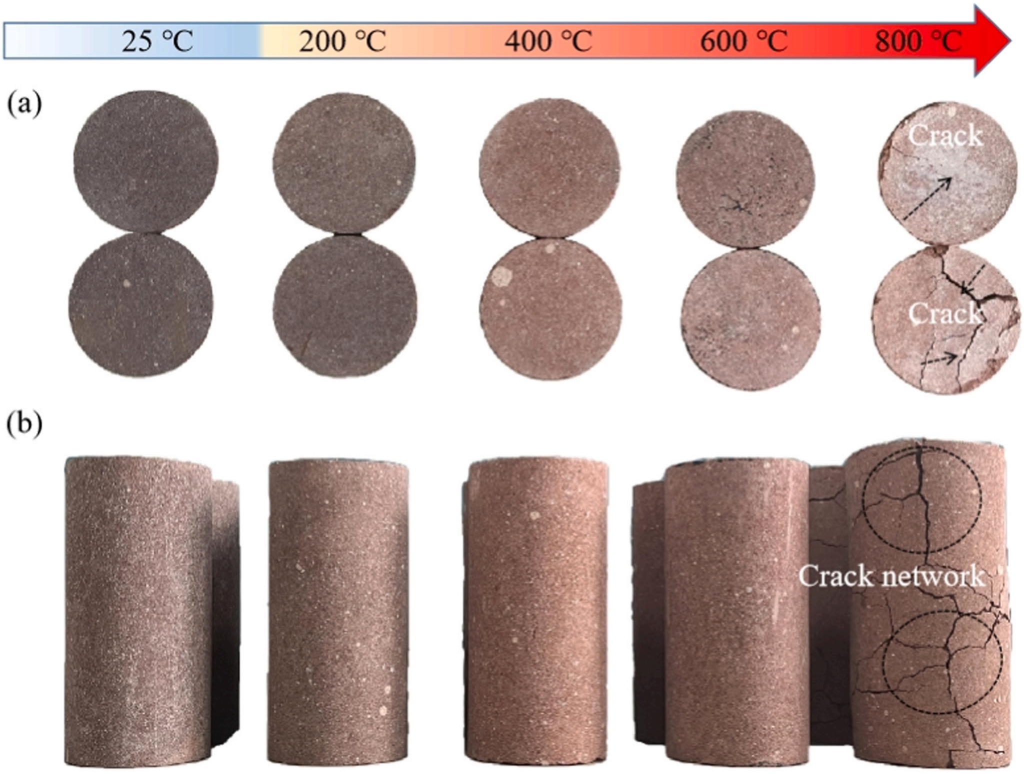

**Fig. 5.** Apparent color and crack evolution of red sandstone after high temperature.

include: 32 cumulative sampling counts, 2048 echoes, 204,828 sampling points per echo, and an echo time of 0.1 ms. Uniaxial compression and Brazilian splitting tests were conducted on a TAW-2000 device. This equipment has a maximum load capacity of 2000 kN, a displacement measurement error $\leq \pm 1$ %, and a deformation measurement error $\leq \pm 0.5$ %. Load was applied using displacement control mode at a rate of 0.01 mm/s. Finally, a Nikon CI-POL polarizing microscope (Japan) with 500 × magnification was used to observe the microstructure of the thermally treated sandstone, obtaining mineral composition and crack distribution patterns.

## 3. Results and analysis

### 3.1. Physical properties

#### 3.1.1. Apparent characteristics

The color changes and surface cracks of red sandstone after different high-temperature treatments are shown in Fig. 5. Below 200 °C, the sandstone specimens remain red, as the primary process is free water dehydration, with negligible changes in surface color and volume. When the peak temperature rises to 800 °C, chemical reactions occur, oxidizing Fe$^{2+}$ ions to Fe$^{3+}$ ions, resulting in a gradual transition of the surface color to brick-red, accompanied by blackened particles. Observations from the top and front views of the captured samples reveal irregular and non-uniform crack distribution. Specifically, no significant cracks are observed on the sandstone surface below 600 °C, whereas at 800 °C, numerous cracks appear. Under high-temperature conditions, substantial thermal stress induces crack initiation and propagation from the specimen center, forming interconnected crack networks. Two dominant axial-parallel cracks are observed, along with spalling fragments near these cracks and specimen ends. Notably, specimens treated at 800 °C were excluded from subsequent mechanical tests due to severe structural damage.

#### 3.1.2. Mass loss and longitudinal wave velocity

High temperatures alter the mass and longitudinal wave velocity of sandstone. Given the small mass variations across temperature groups, mass loss rate ($K_M$) and wave velocity attenuation rate ($K_P$) were adopted to characterize these changes [28,29]. The calculation formula is as follows:

$$R_V = \frac{\Delta V}{V} \times 100\% \tag{1}$$

where $\Delta V$ represents the rate of change in physical parameters, and $V_0$ denotes the initial values of the parameters.

As shown in Fig. 6a, both mass loss rate and wave velocity attenuation rate increase with temperature. In the range of 25–200 °C, the mass loss rate of sandstone remains minimal at 0.069 %. At 800 °C, the mass loss rate ranges from 0.069 % to 3.53 %, representing a 51-fold increase compared to room temperature. The primary reasons are as follows: At lower temperatures (25–200 °C), free water within the sandstone vaporizes and escapes [30], resulting in minimal mass changes. At 400 °C, kaolinite begins to dehydrate, further increasing the mass loss rate. At 573 °C, the quartz phase transition ($\alpha \rightarrow \beta$) induces volumetric expansion, generating internal stresses. When these stresses exceed the stiffness of mineral grains, cracks initiate, propagate, and interconnect, leading to structural deterioration. At 800 °C, surface fragmentation causes significant mass loss.

Longitudinal wave velocity serves as an acoustic indicator for evaluating rock damage and crack development. At room temperature, the average longitudinal wave velocity of sandstone is 2134 m/s. With increasing temperature, the wave velocity decreases progressively (Fig. 6b): At 200°C, the velocity decreases by 2.55 % compared to room temperature. At 400°C, 600°C, and 800°C, the reductions are 6.84 %, 34.51 %, and 48.57 %, respectively. The decline in wave velocity is attributed to thermal stress-induced boundary and transgranular cracks, which compromise rock integrity. Additionally, the escape of free water and evaporation of structural water at elevated temperatures increase porosity and crack density. The resulting structural deterioration obstructs stress wave propagation, causing energy attenuation and reduced

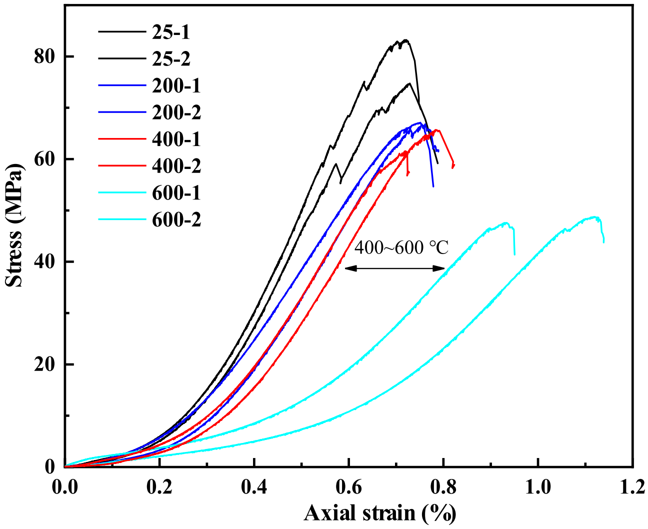

**Fig. 7.** Stress-strain curve of sandstone after high temperature treatment.

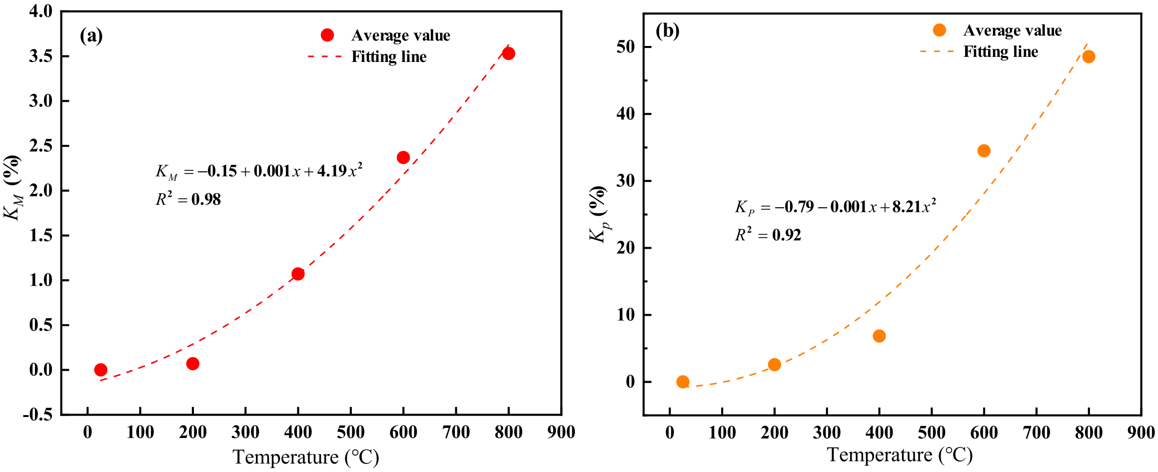

**Fig. 6.** The variation of mass and p-wave velocity with temperature.

wave velocity [31].

### 3.2. Mechanical properties

Fig. 7 shows the axial stress-strain curves of red sandstone after high-temperature treatments (200 °C, 400 °C, 600 °C). Similar to the room-temperature (RT) specimens, the stress-strain curves of thermally treated samples also exhibit five typical stages: compaction stage, elastic deformation stage, stable crack propagation stage, unstable crack propagation stage, and post-peak failure stage [32]. During the initial loading phase, the curve exhibits an upward-concave nonlinear growth due to the closure of internal pores and microcracks in the rock. As temperature increases, the duration of the compaction stage significantly prolongs (Fig. 7), indicating that high temperatures lead to an increase in the number of microcracks [33]. After the closure of microcracks, the curve enters the linear elastic stage, and the elastic modulus can be calculated from the slope of this segment. With continued axial strain, the curve deviates from linearity and enters the yielding stage, during which new microcracks gradually accumulate inside the specimen. When the stress reaches the yield strength, cracks enter the unstable propagation stage, rapidly interconnecting to form macroscopic fracture surfaces, and the curve drops sharply until the specimen is completely destroyed.

Peak strength, elastic modulus, and peak strain of the sandstone were extracted from the stress-strain curves (Table 2, Fig. 8). The results show that as temperature increases, the uniaxial compressive strength, elastic modulus, and tensile strength all exhibit a decreasing trend, while the peak strain gradually increases. Specifically: From 25°C to 200°C: The compressive strength and elastic modulus decrease rapidly by 15.31 % and 21.53 %, respectively, while the peak strain increases slightly by 4.14 %. During this stage, water escape promotes microcrack propagation but does not significantly damage the mineral skeleton. From 200°C to 400°C: The changes in mechanical parameters slow (compressive strength decreases by 19.56 %, elastic modulus by 22.46 %, and peak strain increases by 3.45 %). This is mainly because the adsorbed water inside the specimen has completely escaped, and the mineral components undergo no chemical changes, only slight thermal expansion under temperature effects.

When the temperature rises from 400°C to 600°C, the compressive strength and elastic modulus plummet by 39.04 % and 55.68 %, respectively, while the peak strain surges by 36.55 %. During this stage, the quartz $\alpha \rightarrow \beta$ phase transition (573°C) in the main components of the specimen causes volumetric expansion, leading to a sharp increase in internal stresses between mineral particles [34]. This results in the generation and interconnection of numerous cracks, significantly deteriorating the sandstone structure. Additionally, when the temperature reaches 400°C, kaolinite begins to dehydrate, further promoting the formation of microcracks and reducing the specimen strength. Notably, the tensile strength decreases approximately linearly from 25°C to 600°C without a clear threshold, indicating that its degradation is controlled by the continuous processes of cementation weakening and uniform microcrack propagation.

### 3.3. Pore structure

Nuclear magnetic resonance (NMR) technology primarily utilizes the relaxation properties of hydrogen-containing fluids in rock pores, including bulk relaxation time, surface relaxation time, and diffusion relaxation time. After saturation treatment, the rock is subjected to CPMG (Carr-Purcell-Meiboom-Gill) pulse sequence testing to obtain decay signal values. This signal is a superposition of signals emitted by pores of different sizes within the rock. The spin-echo decay curve can be fitted with a set of exponential decay curves, each with a distinct decay constant. The collection of these constants constitutes the $T_2$ spectrum distribution of NMR. The area under a $T_2$ spectral peak represents the number of pores of that specific size [35,36].

$$\frac{1}{T_2} = \frac{1}{T_{2B}} + \frac{1}{T_{2S}} + \frac{1}{T_{2D}} \tag{2}$$

where, $T_2$ represents the total relaxation time, $T_{2B}$ represents the volume relaxation time, $T_{2S}$ represents the surface relaxation time, and $T_{2D}$ represents the diffusion relaxation time, respectively [37].

$$\frac{1}{T_2} = \rho\left(\frac{S}{V}\right) = \rho\frac{F_S}{r} \tag{3}$$

$$r = T_2 F_S \rho \tag{4}$$

In these equations, $\rho$ is the transverse surface relaxivity coefficient of the rock (typically 1–10 μm/s), $S$ is the pore surface area, $V$ is the pore volume, $F_S$ is the pore shape coefficient (1, 2, and 3 for planar, cylindrical, and spherical pores, respectively), and $r$ is the pore radius [38].

From Eq. (3), it is evident that the pore radius r is proportional to $T_2$. Therefore, the pore radius distribution of the rock can be derived by

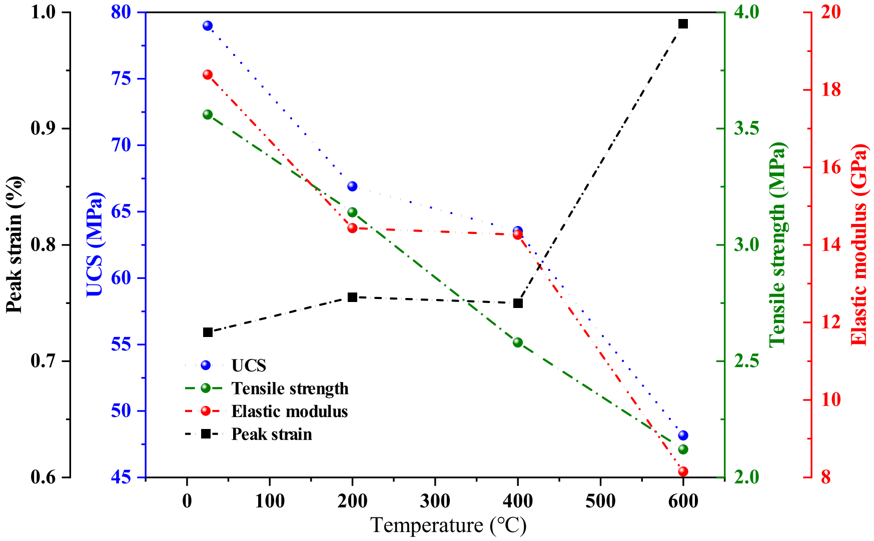

**Fig. 8.** Variations of sandstone mechanical parameters with temperature.

converting $T_2$ values. A systematic classification method divides pores into four types: micropores ($r \le 0.1$ μm), mesopores (0.1 μm$\le r \le 1$ μm, macropores (1 μm$\le r \le 10$ μm), and fractures ($r \ge 10$ μm) [39].

### 3.3.1. T₂ spectra and pore size distribution

The $T_2$ spectra of sandstone samples after different temperature treatments are shown in Fig. 9. All $T_2$ spectral curves exhibit smooth, continuous bimodal distributions, indicative of a typical normal distribution. This suggests that the sandstone has a continuous pore size distribution. At temperatures below 600 °C, the peak positions slightly shift to the right, and the peak amplitudes increase significantly compared to untreated samples. At 800 °C, the first peak shifts markedly to the right, and its intensity increases sharply. This indicates that thermally induced cracks gradually initiate, propagate, and interconnect within the sandstone as temperature rises, leading to an increase in the number of pores corresponding to this peak. Overall, the $T_2$ spectra of thermally treated sandstone reflect the evolutionary patterns of pore structure. The area under the $T_2$ spectral curve increases with temperature, demonstrating that elevated thermal stress promotes pore development.

From Eq. (4), the pore radius of the rock is proportional to the $T_2$ value. Thus, the pore size distribution can be determined from $T_2$ values. The pore size distributions of sandstone after different temperature treatments are shown in Fig. 10. The results reveal that sandstone pores consist primarily of micropores, mesopores, and macropores, with mesopores dominating and fractures being the least prevalent. This demonstrates a multi-scale pore size distribution in sandstone. The proportion of micropores decreases with increasing temperature, while the proportion of mesopores increases.

### 3.3.2. Porosity variation

Fig. 11 shows the NMR porosity of sandstone samples under different temperature treatments. The porosity evolution can be divided into three stages: 25–200°C, 200–600°C, and 600–800°C. The average porosity of untreated sandstone is 3.65 %, indicating that sandstone is a complex porous medium. At 200 °C, porosity increases to 3.90 %, a 6.41 % increment, suggesting limited pore expansion due to the escape of adsorbed and interlayer water. When the temperature rises from 200 °C to 600°C, porosity increases from 3.90 % to 7.25 %, a 46.21 % increase. This significant expansion is attributed to the combined effects of thermal expansion of mineral particles and pore dilation caused by the quartz $\alpha \rightarrow \beta$ phase transition. Above 600 °C, porosity rises sharply to 18.70 % (a 61.23 % increase), driven by accelerated crack development due to continued quartz phase transition and calcite decomposition at 750°C [40]. In summary, sandstone porosity exhibits a periodic variation with temperature, and 600°C serves as a critical threshold for abrupt porosity changes.

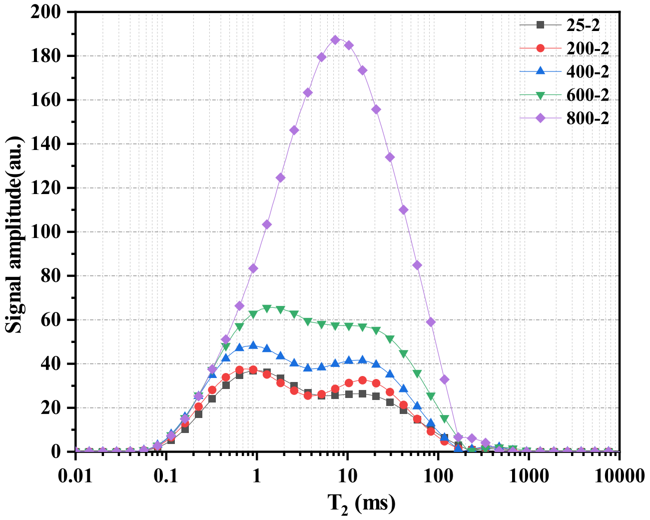

**Fig. 9.** $T_2$ spectral morphology of sandstone with different temperature.

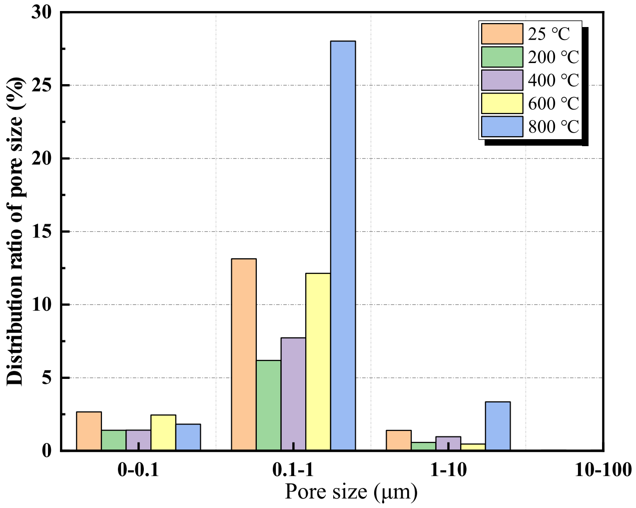

**Fig. 10.** Proportion of pore size distribution at different temperatures.

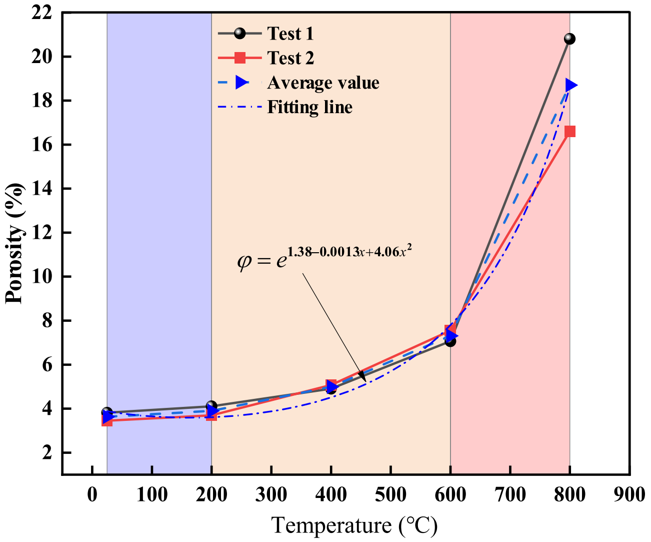

**Fig. 11.** The variation of porosity with temperature.

### 3.3.3. Fractal characteristics

Fractal theory effectively characterizes the fractal features of pore structures. Fractal dimensions quantitatively describe the complexity of pore structures in thermally damaged sandstone and reveal their evolution under different thermal conditions [41,42]. The formula for fractal dimension is:

$$\lg(S_v) = (3-D)\lg(T_2) + (D-3)\lg(T_{2\max}) \tag{5}$$

Due to the bimodal shape of the $T_2$ spectrum, the relationship between $\lg(S_v)$ and $\lg(T_2)$ can be divided into three segments corresponding to micropores, mesopores, and macropores. The left side of the peak curve corresponds to micropores, the right side to macropores, and the remaining curve to mesopores. The fractal dimensions of these three segments are denoted as $D_s$, $D_m$, and $D_b$, respectively. The total fractal dimension of the $T_2$ spectrum is denoted as $D_t$. Fig. 12 shows the lg ($T_2$) vs. lg ($S_v$) relationship for untreated high-temperature samples, while the fractal dimensions $D_s$, $D_m$, $D_b$, and $D_t$ are illustrated in Fig. 13. The

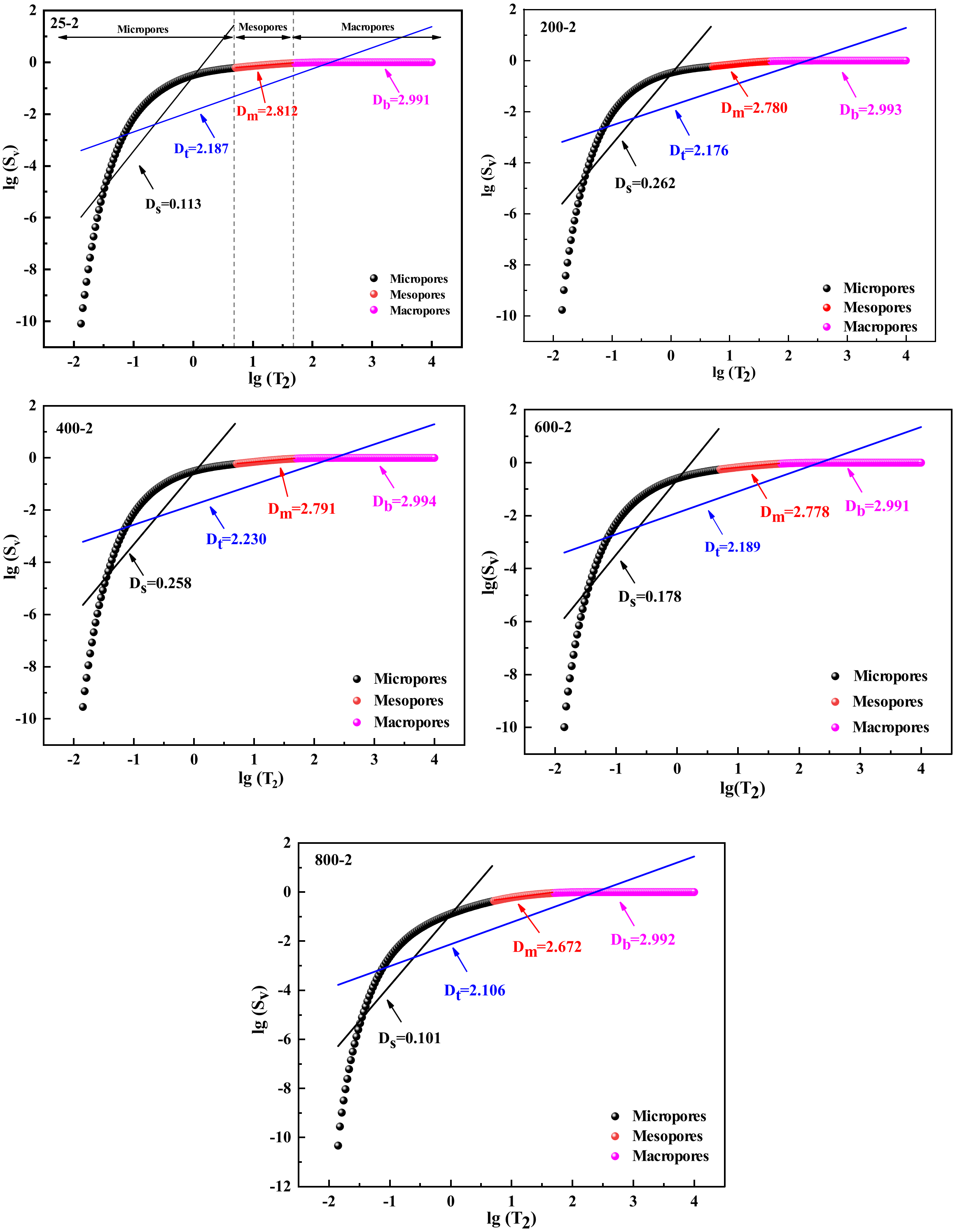

**Fig. 12.** Evolution of fractal characteristics in $T_2$ spectra of sandstone under different temperature treatments.

fractal dimensions of sandstone pores under different temperature treatments are listed in Table 1. Generally, the fractal dimension in three-dimensional geometric space ranges from 2 to 3. For small pores in sandstone, fractal dimensions range from 0.101 to 0.262, indicating that some micropores lack typical fractal characteristics. In contrast, mesopores and macropores exhibit fractal dimensions between 2.672 and 2.994, demonstrating clear fractal behavior. These results indicate that the pore structure of thermally treated sandstone exhibits distinct fractal characteristics. Furthermore, the calculated fractal dimensions vary significantly with the selected pore size ranges, suggesting that sandstone pore structures possess multifractal features.

After high-temperature treatment, the fractal dimension of macropores approaches 3, reflecting their complexity and heterogeneity. The fractal dimension of mesopores ranges from 2.6 to 2.8, slightly lower

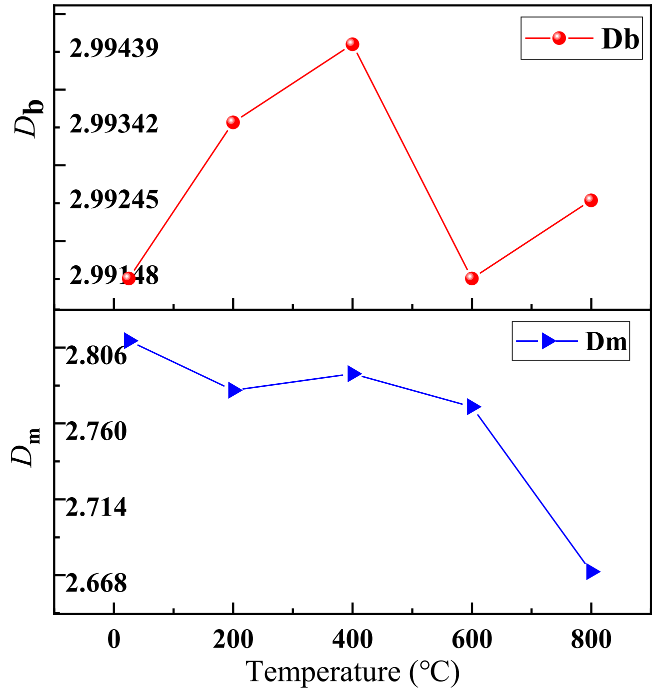

**Fig. 13.** The relationship between the fractal dimension of macropores and mesopores and temperature.

**Table 1**
Pore fractal dimensions of different thermal-treated sandstone.

| No. | Fractal dimensions | | | |
|---|---|---|---|---|
| | $D_s$ | $D_m$ | $D_b$ | $D_t$ |
| 25–2 | 0.113 | 2.812 | 2.991 | 2.187 |
| 200–2 | 0.262 | 2.780 | 2.993 | 2.176 |
| 400–2 | 0.258 | 2.791 | 2.994 | 2.230 |
| 600–2 | 0.178 | 2.778 | 2.991 | 2.189 |
| 800–2 | 0.101 | 2.672 | 2.992 | 2.106 |

than that of macropores, indicating better uniformity and lower complexity [43]. With increasing temperature, the fractal dimension of macropores shows a dynamic "increase-decrease" trend, albeit with minimal rate changes. Conversely, the fractal dimension of mesopores gradually decreases with temperature and drops abruptly at 600 °C.

## 4. Discussion

### 4.1. Thermal damage mechanisms

Different minerals in rocks have distinct thermal expansion coefficients, leading to intragranular and transgranular cracks at various locations and orientations [44]. When rocks are subjected to temperature, thermal stress arises due to mismatched mineral expansion. Once the thermal stress exceeds the bonding strength between or within minerals, microcracks form. To visually observe microstructural changes in sandstone after high-temperature treatment, polarized light microscopy was used to examine the microstructure of sandstone treated at different temperatures (Fig. 14). Before thermal treatment, mineral grains in the samples are densely packed and intact, with larger grain sizes. Quartz dominates the composition, accompanied by minor microcline, albite, and kaolinite. ImageJ analysis (cracks marked in red) reveals that the crack area at this stage is only 1.86 %. At 200 °C, the tight arrangement of mineral grains loosens, and larger pores form between grains, due to moisture escape. At this stage, thermal expansion effects are not fully developed, and only discrete microcracks appear within grains or at interfaces (crack area increases to 5.03 % in Fig. 14).

When the temperature rises to 400 °C, intensified thermal expansion reduces the number of large intergranular pores. Under thermal stress, intragranular and intergranular cracks proliferate, and localized mineral fragmentation occurs, reducing overall grain size (As shown in Fig. 14, the fracture area proportion in cast thin sections observed under optical microscopy has increased to 10 %.). At 600 °C, the primary mineral component, quartz, undergoes an $\alpha\rightarrow\beta$ phase transition (threshold temperature: 573 °C). Post-transition quartz exhibits increased volume and stiffness, generating significant internal expansion stress [45]. This stress accelerates crack propagation and interconnection, forming a network of fractures. Concurrently, microcline begins to decompose at 600 °C, resulting in finer quartz and microcline grains (Fig. 14), with crack area reaching 11.9 %. At 800 °C, calcite decomposes (threshold temperature: 750 °C), and $CO_2$ released during decomposition loosens the pore structure. The specimen becomes fragile and structurally compromised under thermal stress, with internal decomposition pores visible in Fig. 14. Crack area further increases to 14.66 %.

### 4.2. Fractal dimension and pore structure relationship

Thermal damage at high temperatures alters rock pore structure, which in turn critically influences physical and mechanical properties. This study identifies intrinsic correlations between compressive strength, elastic modulus, and the quantity and fractal dimension of macropores, as well as between tensile strength and the quantity and fractal dimension of mesopores. Macropores primarily originate from mineral grain gaps or main crack extensions [46]. Across temperature-treated specimens (excluding the 800 °C group),

**Table 2**
Basic physical parameters of red sandstone before and after high-temperature treatment.

| No. | Physical parameters | | | | Mechanical parameters | | | |
|---|---|---|---|---|---|---|---|---|
| | Mass (g) | P-wave velocity (m/s) | Porosity (%) | Crack area (%) | UCS (MPa) | BTS (MPa) | Elastic modulus (GPa) | Peak strain (%) |
| 25–1 | 449.64 | 2085.00 | 3.81 | 1.51 | 83.24 | 3.51 | 18.96 | 0.72 |
| 25–2 | 435.58 | 2183.00 | 3.45 | 2.21 | 74.75 | 3.60 | 17.81 | 0.73 |
| 200–1 | 434.61 | 2109.00 | 4.10 | 4.76 | 66.80 | 3.54 | 14.61 | 0.76 |
| 200–2 | 451.22 | 2050.00 | 3.69 | 5.30 | 67.00 | 2.73 | 14.25 | 0.75 |
| 400–1 | 437.27 | 2098.00 | 4.90 | 7.11 | 65.51 | 2.55 | 14.79 | 0.78 |
| 400–2 | 439.07 | 1878.00 | 5.07 | 12.89 | 61.56 | 2.60 | 13.73 | 0.72 |
| 600–1 | 432.10 | 1400.00 | 7.06 | 14.62 | 47.57 | 2.02 | 8.20 | 0.93 |
| 600–2 | 432.70 | 1395.00 | 7.55 | 11.19 | 48.72 | 2.22 | 8.10 | 1.05 |
| 800–1 | 426.14 | 1125.00 | 20.81 | 16.62 | / | / | / | / |
| 800–2 | 428.43 | 1070.00 | 16.61 | 12.70 | / | / | / | / |

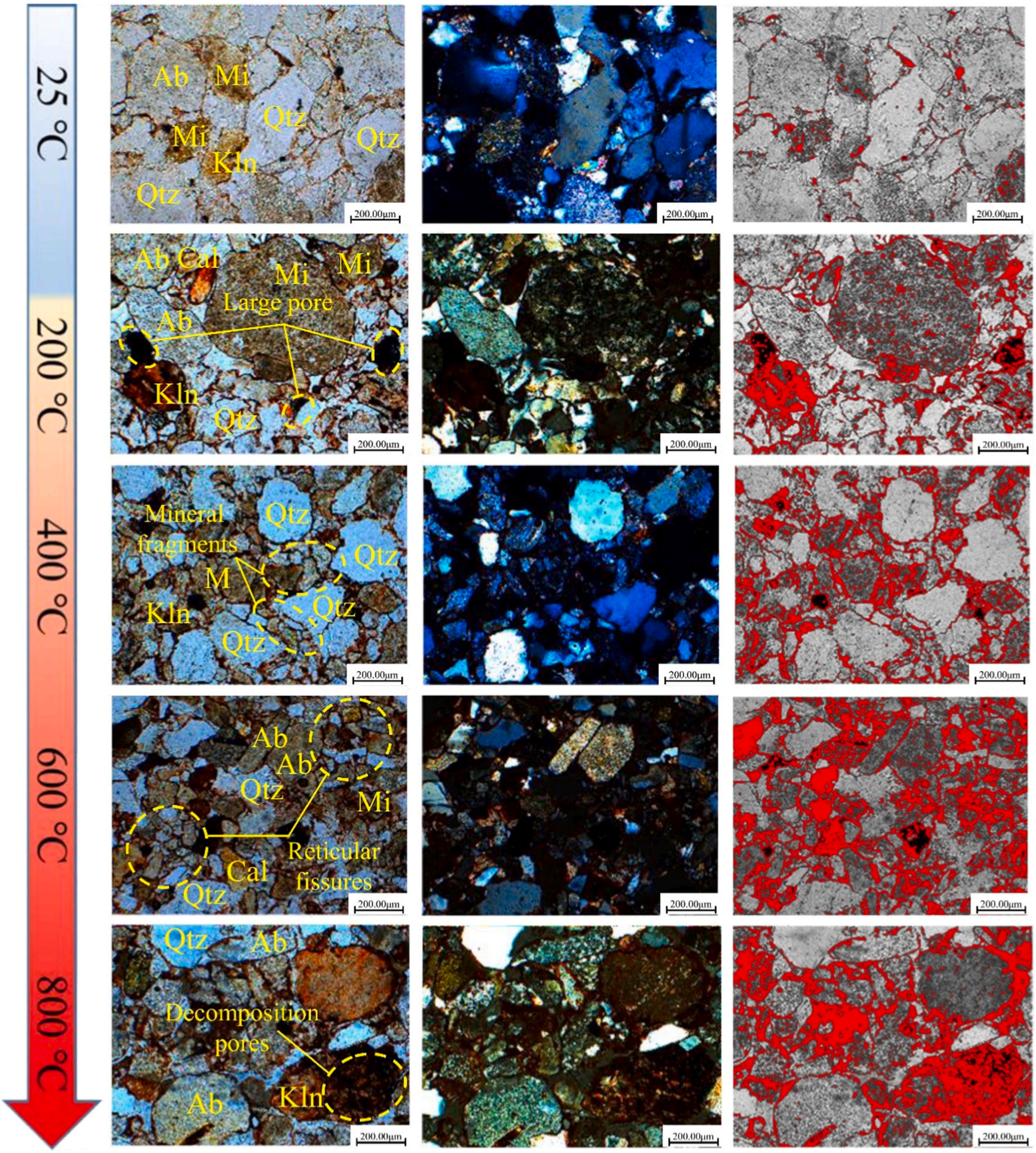

**Fig. 14.** Microscopic thin section observation results of sandstone samples.

macropores remain the least abundant among the three pore types. (1) 25–200 °C: Slight thermal expansion of minerals reduces macropore quantity; (2) 400 °C: Increased thermal stress promotes microcrack development, slightly increasing macropores; (3) 600 °C: Quartz phase transition drives rapid crack growth, with some macropores expanding into larger pores, reducing macropore count; (4) 800 °C:Thermal stress and calcite decomposition-induced $CO_2$ release synergistically cause macropore proliferation.

The fractal dimension ($D_b$) of macropores remains near 3 across all temperatures, reflecting their structural complexity and heterogeneity. Irregular geometries induce localized stress concentrations, facilitating crack network formation. Below 600 °C, ongoing microcrack development under thermal stress gradually increases macropore complexity, with $D_b$ showing a slow upward trend. At 573 °C, quartz phase transition-induced volumetric expansion generates intense thermal stress [47], rapidly interconnecting macropores into simplified fracture-dominated structures, slightly lowering $D_b$. By 600 °C, quartz phase transition completes, but at 800 °C, calcite decomposition releases $CO_2$ [48], causing pore wall disintegration. Secondary crack branching and tortuosity enhance pore heterogeneity, restoring $D_b$. Comparative analysis reveals that $D_b$ synchronizes with the staged degradation of compressive strength and elastic modulus from 25 °C to 600 °C: 25 °C–200 °C: Thermal expansion mismatch induces microcrack branching, rapidly increasing macropore complexity and stress concentration, leading to sharp declines in compressive strength and elastic modulus. 200 °C–400 °C: Saturated thermal expansion slows crack propagation, reducing the rate of macropore complexity growth and mechanical degradation.400 °C–600 °C: Quartz phase transition simplifies pore structure via main crack interconnection, causing $D_b$ to drop abruptly. However, overall pore network deterioration drives drastic reductions in compressive strength and elastic modulus.

Mesopores mainly consist of intergranular pores or tiny cracks formed by cementation loss. Mesopores dominate across all temperature-treated specimens. 25°C–200°C: Minor thermal expansion of minerals slightly reduces mesopore quantity. 200°C–600°C: Intergranular microcrack development steadily increases mesopores. Notably, mesopore counts at 600°C remain slightly below initial levels, suggesting that mesopore expansion in this range results from thermal expansion-induced grain compression.800°C: Calcite decomposition between 600°C and 800°C leaves residual pores, drastically increasing mesopores.

The fractal dimension of mesopores ($D_m$) decreases linearly from 2.812 (initial) to 2.672 (800 °C), reflecting reduced complexity due to enhanced pore connectivity. At 600 °C, $D_m$ remains stable, unlike $D_b$, as stronger intergranular cementation delays structural reorganization. At 750 °C, calcite decomposition and $CO_2$ escape weaken cementation, forming a more regular mesopore network. The linear decline of $D_m$ from 25 °C to 600 °C parallels tensile strength degradation, indicating progressive cementation weakening and tensile crack propagation along regularized pore paths.

### 4.3. Damage variables

The changes in mineral composition and pore structure of sandstone specimens are reflected in their macroscopic mechanical properties. The reduction rates of P-wave velocity, compressive strength, tensile strength, elastic modulus, and porosity of sandstone after high-temperature treatment are used to characterize the damage variables. Assuming the damage is entirely caused by temperature on the sandstone specimens, meaning the damage variable value of sandstone specimens in their initial state is zero, the formula for calculating the damage variable of sandstone after high-temperature treatment is as follows:

$$D_P = \frac{V_0 - V_t}{V_0} \tag{6}$$

$$D_{UCS} = \frac{\sigma_0 - \sigma_t}{\sigma_0} \tag{7}$$

$$D_{BTS} = \frac{\tau_0 - \tau_t}{\tau_0} \tag{8}$$

$$D_E = \frac{E_0 - E_t}{E_0} \tag{9}$$

In the formula, $V_0$, $\sigma_0$, $\tau_0$, and $E_0$ represent the P-wave velocity, compressive strength, tensile strength, and elastic modulus without heat treatment, respectively; $V_t$, $\sigma_t$, $\tau_t$, and $E_t$ represent the P-wave velocity, compressive strength, tensile strength, and elastic modulus after different temperature treatments, respectively.

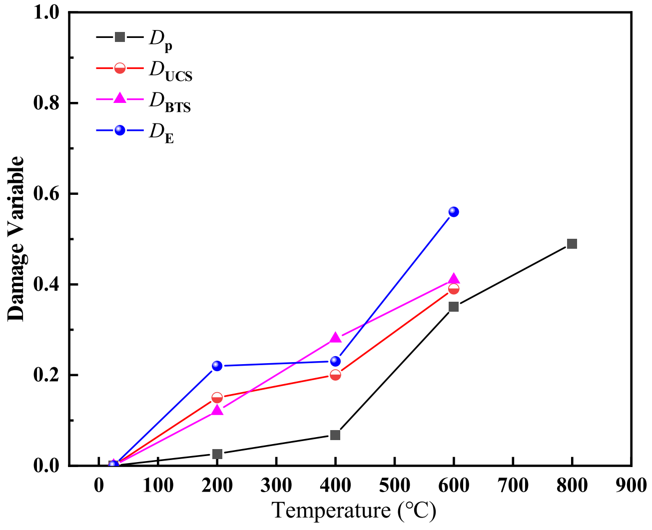

**Fig. 15.** Damage variables based on physical and mechanical parameters.

The evolution patterns of various damage variables at different temperatures are shown in Fig. 15, demonstrating stage characteristics that are highly coupled with the thermal damage mechanisms of sandstone. In this study, the initial uniaxial compressive strength of untreated sandstone was 8.9 MPa with a porosity of 3.63 %, exhibiting typical mechanical properties of hard rock. As the heat treatment temperature increases, $D_{UCS}$, $D_E$, $D_{BTS}$ and $D_P$ all show significant temperature dependence. Using 200 °C, 400 °C and 600 °C as threshold values, the process can be divided into four stages:

The evolution of damage variables at different temperatures is shown in Fig. 15, exhibiting stage characteristics highly coupled with sandstone's thermal damage mechanisms. The initial uniaxial compressive strength of untreated sandstone in this study was 8.9 MPa with 3.63 % porosity, demonstrating typical hard rock mechanical properties. As heating temperature increases, $D_{UCS}$, $D_E$, $D_{BTS}$ and $D_P$ all show significant temperature dependence. Using 200 °C, 400 °C and 600 °C as thresholds, the process can be divided into four stages: Below 200 °C, $D_{UCS}$ and $D_E$ increase rapidly at rates of 15.31 % and 21.51 % respectively. Damage mainly originates from discrete pores formed by adsorbed water escape and microcrack branching caused by initial thermal expansion of mineral particles. Despite significant mechanical parameter deterioration, thin-section observations reveal fracture area only increases to 5.03 %, indicating mineral framework maintains structural integrity. From 200 °C to 400 °C, the growth rates of $D_{UCS}$ and $D_E$ slow significantly, reflecting saturation of mineral thermal expansion. The mesopore fractal dimension $D_m$ decreases from 2.812 to 2.782, suggesting thermal compaction promotes regular arrangement of intergranular pores, inhibiting disordered crack propagation. Notably, $D_{BTS}$ continues linear growth, revealing progressive thermal decomposition of cementing materials (kaolinite, calcite) dominates tensile failure path formation. Between 400 °C and 600 °C, quartz's $\alpha \rightarrow \beta$ phase transition (573 °C) triggers abrupt damage: $D_{UCS}$ and $D_E$ surge by 19.34 % and 33.23 % respectively, corresponding to porosity increase from 4.99 % to 7.25 % and thin-section fracture area exceeding 11.9 %. Slight decrease in macropore fractal dimension $D_b$ indicates main crack network interconnection and reconstruction, temporarily reducing pore topology complexity while significantly enhancing connectivity, ultimately causing cliff-like compressive capacity deterioration. Above 600 °C, $D_P$ growth slows because although $CO_2$ escape pores from calcite decomposition intensify structural loosening, macroscopic fragmentation has completely disrupted stress wave propagation paths. $D_{BTS}$ maintains linear growth, quantitatively correlating with continuous $D_m$ decrease, highlighting tensile failure being cross-scale driven by cement weakening-pore regularization. At 800 °C, specimens show macroscopic fragmentation structure, losing basic mechanical testing conditions.

## 5. Conclusion

The physico-mechanical properties and pore structure characteristics of sandstone after high temperature were studied through laboratory experiments, the thermal damage mechanism of sandstone and the relationship between pore structure and fractal dimension were explored. The main conclusions are as follows:

(1) The behavior of sandstone samples under varying temperatures reveals distinct threshold points at 200 °C and 400 °C. Below 200 °C, the properties of the sandstone remain relatively stable, showing minimal changes in color, cracks, longitudinal wave velocity, and mass loss. However, significant transformations occur as the temperature rises from 200 to 400 °C. The mass loss rate and longitudinal wave velocity of the sandstone samples experience notable increments, along with a shift in color from dark red to brick red on the surface. With a further increase in

temperature from 400 to 800 °C, the sandstone samples undergo more pronounced changes.

(2) The physical properties of sandstone specimens exhibit three threshold temperatures: 200 °C, 400 °C, and 600 °C. During 25–200 °C, combined effects of adsorbed/interlayer water escape and initial thermal expansion of mineral grains cause rapid reduction in compressive strength and elastic modulus. From 200–400 °C, thermal expansion saturation significantly slows deterioration rates. Specimen surfaces transition to brick-red with extended intragranular cracks under sustained thermal stress, while mineral cementation remains intact. The 400–600 °C stage demonstrates abrupt mechanical property deterioration due to quartz phase transition.

(3) NMR and fractal analyses reveal temperature-dependent evolution of pore structure. From 25–600 °C, large-pore fractal dimension $D_b$ shows inverted U-shaped variation: initial $D_b$= 2.991 at room temperature peaks at 2.994 (400 °C) reflecting enhanced crack branching complexity and pore heterogeneity, then slightly decreases to 2.991 (600 °C) as quartz phase transition causes crack network interconnection that simplifies pore topology while maintaining secondary crack complexity. Medium-pore fractal dimension $D_m$ decreases linearly from 2.812 (25 °C) to 2.778 (600 °C), ultimately reaching 2.672 at 800 °C.

(4) The high-temperature deterioration mechanism of sandstone is governed by synergistic effects of mineral phase transitions and pore-cement interactions. Quartz $\alpha \rightarrow \beta$ phase transition generates internal stresses exceeding mineral stiffness through volumetric expansion, accelerating microcrack propagation and interconnection to form transgranular crack networks that directly cause compressive strength collapse and elastic modulus degradation. Kaolinite dehydration and calcite decomposition weaken intergranular cementation, quantitatively reflected by linear decrease of medium-pore fractal dimension $D_m$.

(5) Thermal expansion coefficient differences among quartz, feldspar, and calcite generate shear stresses at grain boundaries, preferentially inducing intergranular cracks before stress transfers intragranularly, causing feldspar edge fragmentation and quartz intragranular crack initiation. Post-600 °C, phase transitions and cement weakening jointly drive crack evolution from localized damage to transgranular networks, creating multi-scale failure systems integrating micron-scale pores, mesoscopic cracks, and macroscopic fractures.

## CRediT authorship contribution statement

**Junqiao Yu:** Writing – original draft. **Yun Wu:** Writing – original draft, Funding acquisition. **Jiamin Wang:** Software, Conceptualization. **Lei Wang:** Software, Data curation. **Lihua Hu:** Formal analysis, Data curation. **Jian Lin:** Methodology, Formal analysis.

## Declaration of Competing Interest

The authors declare that they have no known competing financial interests or personal relationships that could have appeared to influence the work reported in this paper.

## Acknowledgments

The authors gratefully acknowledge the National Natural Science Foundation of China (No. 42307244 and 42230704), Xuzhou Research Program Youth Science and Technology Project (KC23044), Open Fund of State Key Laboratory of Geological Disaster Prevention and Geological Environment Protection (SKLGP2024K022).

## Data Availability Statement

Data sharing is not applicable to this study because no new data were generated.

## References

[1] J. Zhu, T. Qi, J.R. Li, et al., The effects of high temperature on crack propagation and failure characteristics of sandstone, Rock Mech. Rock Eng. 56 (2023) 5753–5779, https://doi.org/10.1007/s00603-023-03356-6.
[2] S.V. Pathiranagei, I. Gratchev, R. Kong, Engineering properties of four different rocks after heat treatment, Geomech. Geophys. Geo-Energy Geo-Resour. 7 (1) (2021) 1–12, https://doi.org/10.1007/s40948-020-00211-8.
[3] T. Meng, R.C. Liu, X.X. Meng, et al., Evolution of the permeability and pore structure of transversely isotropic calcareous sediments subjected to triaxial pressure and high temperature, Eng. Geol. 253 (2019) 27–35, https://doi.org/10.1016/j.enggeo.2019.03.007.
[4] A.W. Bhutto, A.A. Bazmi, G. Zahedi, Underground coal gasification: From fundamentals to applications, Prog. Energy Combust. Sci. 39 (1) (2013) 189–214, https://doi.org/10.1016/j.pecs.2012.09.004.
[5] Y. Wu, X.Z. Li, Z. Huang, et al., Effect of temperature on physical, mechanical and acoustic emission properties of Beishan granite, Gansu Province, China, Nat. Hazards 107 (2021) 1577–1592.
[6] Z. Huang, W. Zeng, Y. Wu, et al., Effects of temperature and acid solution on the physical and tensile mechanical properties of red sandstones, Environ. Sci. Pollut. Res. 28 (16) (2021) 20608–20623, https://doi.org/10.1007/s11356-020-11866-x.
[7] L.C. Deng, X.Z. Li, Y. Wu, et al., Influence of cooling speed on the physical and mechanical properties of granite in geothermal-related engineering, Deep Undergr. Sci. Eng. 1 (1) (2022) 40–57, https://doi.org/10.1002/dug2.12011.
[8] L. Zhou, Z.D. Zhu, E. Oterkus, et al., Research on the effects of heating and cooling processes on the mechanical properties of yellow rust granite, Geohazard Mechanics 1 (3) (2023) 231–243, https://doi.org/10.1016/j.ghm.2023.09.001.
[9] M. Li, X.S. Liu, Effect of thermal treatment on the physical and mechanical properties of sandstone: Insights from experiments and simulations, Rock Mech. Rock Eng. 55 (2022) 3171–3194, https://doi.org/10.1007/s00603-022-02791-1.
[10] C. Otto, T. Kempka, Thermo-mechanical simulations confirm: Temperature-dependent mudrock properties are nice to have in far-field environmental assessments of underground coal gasification, Energy Procedia 76 (2015) 582–591.
[11] L. Griffiths, O. Lengliné, M.J. Heap, et al., Thermal cracking in westerly granite monitored using direct wave velocity, coda wave interferometry, and acoustic emissions, J. Geophys. Res. Solid Earth 123 (2018) 2246–2261.
[12] L. Wang, Y. Wu, Z. Huang, et al., Effects of temperature and confining pressure on the permeability of Beishan granite: An experimental study, Case Stud. Therm. Eng. 55 (2024) 104111, https://doi.org/10.1016/j.csite.2024.104111.
[13] W.G.P. Kumari, P.G. Ranjith, M.S.A. Perera, et al., Experimental investigation of quenching effect on mechanical, microstructural and flow characteristics of reservoir rocks: Thermal stimulation method for geothermal energy extraction, J. Pet. Sci. Eng. 162 (2018) 419–433, https://doi.org/10.1016/j.petrol.2017.12.033.
[14] Y.S. Zhao, Z.J. Wang, Z.J. Feng, et al., Evolution of mechanical properties of granite at high temperature and high pressure, Geomech. Geophys. Geo-Energy Geo-Resour. 3 (2) (2017) 199–210.
[15] B. Singh, P.G. Ranjith, D. Chandrasekharam, et al., Thermo-mechanical properties of Bundelkhand granite near Jhansi, India, Geomech. Geophys. Geo-Energy Geo-Resour. 1 (2015) 35–53, https://doi.org/10.1007/s40948-015-0005-z.
[16] Z.X. Liu, Y. Wu, X.Z. Li, et al., Effects of thermal treatment on the macroscopic physical properties and microstructure of Beishan fine-grained granite, Bull. Eng. Geol. Environ. 81 (5) (2022) 190, https://doi.org/10.1007/s10064-022-02673-4.
[17] Y. Wu, L.C. Deng, Z. Huang, et al., Experimental investigation of temperature effects on the physical and mechanical properties of red sandstone, Q. J. Eng. Geol. Hydrogeol. 56 (2023), https://doi.org/10.1144/qjegh2021-086.
[18] P. Zhang, S.F. Tian, S. Ren, et al., Effects of high temperature and acidic solutions on the pore characteristics and mechanical properties of sandstone, Environ. Sci. Pollut. Res. 30 (2023) 21888–21899, https://doi.org/10.1007/s11356-022-23735-w.
[19] W.L. Geng, J.D. Wang, X.C. Zhang, et al., Experimental study of pore structure and rock mechanical properties of tight sandstone after acid treatment, Acta Geotech 18 (2023) 6559–6571, https://doi.org/10.1007/s11440-023-02094-x.
[20] Y. Lin, K.P. Zhou, R.G. Gao, et al., Influence of chemical corrosion on pore structure and mechanical properties of sandstone, Geofluids (2019) 7320536.
[21] B.L.A. Isaka, P.G. Ranjith, T.D. Rathnaweera, et al., Quantification of thermally-induced microcracks in granite using X-ray CT imaging and analysis, Geothermics 81 (2019) 152–167, https://doi.org/10.1016/j.geothermics.2019.04.007.
[22] S. Mayo, M. Josh, Y. Nesterets, et al., Quantitative micro-porosity characterization using synchrotron micro-CT and xenon K-edge subtraction in sandstones, carbonates, shales and coal, Fuel 154 (2015) 167–173.

[23] M.A. Acevedo Zamora, C.E. Schrank, B.S. Kamber, Using the traditional microscope for mineral grain orientation determination: A prototype image analysis pipeline for optic-axis mapping (POAM), J. Microsc. (2024) 1–30, https://doi.org/10.1111/jmi.13284.

[24] L.F. Fan, J.W. Gao, Z.J. Wu, et al., An investigation of thermal effects on micro-properties of granite by X-ray CT technique, Appl. Therm. Eng. 140 (2018) 505–519, https://doi.org/10.1016/j.applthermaleng.2018.05.074.

[25] S.Q. Yang, P.G. Ranjith, H.W. Jing, et al., An experimental investigation on thermal damage and failure mechanical behavior of granite after exposure to different high temperature treatments, Geothermics 65 (2017) 180–197.

[26] P.K. Gautam, A.K. Verma, M.K. Jha, et al., Study of strain rate and thermal damage of Dholpur sandstone at elevated temperature, Rock Mech. Rock Eng. 49 (2016) 3805–3815, https://doi.org/10.1007/s00603-016-0965-5.

[27] N.N. Sirdesai, T.N. Singh, P.R. Gamage, Thermal alterations in the poro-mechanical characteristic of an Indian sandstone—a comparative study, Eng. Geol. 226 (2017) 208–220, https://doi.org/10.1016/j.enggeo.2017.06.010.

[28] B.K. Ram, V. Gupta, Physico-mechanical characterization of Higher Himalayan granite under the thermal treatments of different heating-cooling conditions, Acta Geotech. 19 (2024) 2841–2854, https://doi.org/10.1007/s11440-023-02224-5.

[29] Q. Sun, C. Lü, L.W. Cao, et al., Thermal properties of sandstone after treatment at high temperature, Int. J. Rock Mech. Min. Sci. 85 (2016) 60–66, https://doi.org/10.1016/j.ijrmms.2016.03.006.

[30] C. Lu, Q. Sun, W.Q. Zhang, et al., The effect of high temperature on tensile strength of sandstone, Appl. Therm. Eng. 111 (2017) 573–579, https://doi.org/10.1016/j.applthermaleng.2016.09.151.

[31] H.J. Su, H.W. Jing, X.B. Mao, et al., Size effect of sandstone after high temperature under uniaxial compression, J. Cent. South Univ. 22 (5) (2015) 1901–1908, https://doi.org/10.1007/s11771-015-2709-1.

[32] B. Zhang, H. Tian, B. Dou, et al., Macroscopic and microscopic experimental research on granite properties after high-temperature and water-cooling cycles, Geothermics 93 (2021) 102079, https://doi.org/10.1016/j.geothermics.2021.102079.

[33] B. Mahanta, V. Vishal, N. Sirdesai, et al., Progressive deformation and pore network attributes of sandstone at in-situ stress states using computed tomography, Eng. Fract. Mech. 252 (2021) 107833, https://doi.org/10.1016/j.engfracmech.2021.107833.

[34] B. Mahanta, P.G. Ranjith, V. Vishal, et al., Temperature-induced deformational responses and microstructural alteration of sandstone, J. Pet. Sci. Eng. 192 (2020) 107239, https://doi.org/10.1016/j.petrol.2020.107239.

[35] C. Wang, W.S. Pei, M.Y. Zhang, et al., Multi-scale experimental investigations on the deterioration mechanism of sandstone under wetting-drying cycles, Rock Mech. Rock Eng. 54 (1) (2021) 429–441, https://doi.org/10.1007/s00603-020-02257-2.

[36] K. Long, Q.K. Wei, K. Peng, et al., Cracking process and microstructural characteristics of granite under heating-cooling alternations, Phys. Fluids 36 (3) (2024) 036613, https://doi.org/10.1063/5.0194662.

[37] N. Zhang, Z.Y. Zhang, C.G. Yan, et al., Coupled effects of acid and temperature on the damage characteristics of sandstone, Rock Mech. Rock Eng. 56 (2023) 7839–7859, https://doi.org/10.1007/s00603-023-03465-2.

[38] J.G. Dong, H.B. Lyu, G.Y. Xu, A nuclear magnetic resonance based quantification of pore water distribution in unsaturated soils, Transp, Geotech 38 (2023) 100922, https://doi.org/10.1016/j.trgeo.2022.100922.

[39] Y.J. Chen, T.B. Yin, X.B. Li, et al., Experimental investigation on dynamic mechanical behavior and fracture evolution of fissure-filled red sandstone after thermal treatment, Eng. Geol. 295 (2021) 106433, https://doi.org/10.1016/j.enggeo.2021.106433.

[40] X. Cai, J.F. Yuan, Z.L. Zhou, et al., Strain rate-dependency of thermal infrared radiation of sandstone subjected to dynamic loading: Insights from a lab testing, Int. J. Rock Mech. Min. Sci. 181 (2024) 105855, https://doi.org/10.1016/j.ijrmms.2024.105855.

[41] X.H. Wu, M.F. Cai, Y. Zhu, et al., An experimental study on the fractal characteristics of the effective pore structure in granite by thermal treatment, Case Stud. Therm. Eng. 45 (2023) 102921, https://doi.org/10.1016/j.csite.2023.102921.

[42] X.B. Guo, Z.L. Huang, L.B. Zhao, et al., Pore structure and multi-fractal analysis of tight sandstone using MIP, NMR and NMRC methods: A case study from the Kuqa depression, China, J. Pet. Sci. Eng. 178 (2019) 544–558, https://doi.org/10.1016/j.petrol.2019.03.069.

[43] Y.L. Zhang, Q. Sun, H. He, et al., Pore characteristics and mechanical properties of sandstone under the influence of temperature, Appl. Therm. Eng. 113 (2017) 537–543, https://doi.org/10.1016/j.applthermaleng.2016.11.061.

[44] Y.J. Shen, Y.L. Zhang, F. Gao, et al., Influence of temperature on the microstructure deterioration of sandstone, Energies 11 (7) (2018) 1753, https://doi.org/10.3390/en11071753.

[45] X.X. Fang, C.F. Ma, L.Q. Zhao, et al., Diagenetic evolution of tight sandstone and the formation of an effective reservoir in the lower member 3 of the Shahejie Formation, Bohai Bay Basin, East China, Mar. Pet. Geol. 161 (2024) 106658, https://doi.org/10.1016/j.marpetgeo.2023.106658.

[46] L.W. Wu, Y.L. Huang, J.M. Li, et al., Macro- and micro-mechanical response and damage mechanism of sandstone under high-temperature conditions, Int. J. Min. Sci. Technol. 35 (2) (2025) 265–274, https://doi.org/10.1016/j.ijmst.2025.01.004.

[47] Q. Sun, C. Lü, L.W. Cao, et al., Thermal properties of sandstone after treatment at high temperature, Int. J. Rock Mech. Min. Sci. 85 (2016) 60–66, https://doi.org/10.1016/j.ijrmms.2016.03.006.

[48] H. Zhang, T. Liu, Y. Cui, et al., Experimental study on the deterioration mechanisms of physical and mechanical properties of red sandstone after thermal-acid coupling treatment, Constr. Build. Mater. 455 (2024) 139106, https://doi.org/10.1016/j.conbuildmat.2024.139106.

**Dr. Yun Wu** is an associate professor at China University of Mining and Technology. He obtained his Ph.D. in geological engineering from Nanjing University in 2021. His main research fields include nuclear waste disposal, deep energy storage, and thermal energy exploitation. Dr. Wu has hosted many research projects from the National Natural Science Foundation of China and other institutions, and published more than 70 peer-reviewed papers.